

Searching for X-Shaped Radio Galaxies Hosting Binary Supermassive Blackholes

Emiko Gardiner^{1,2}

Advisors: Ilsang Yoon¹, Bjorn Emonts¹

¹National Radio Astronomy Observatory, 5220 Edgemont Road, Charlottesville, VA 22903, USA; ecg6wm@virginia.edu, iyoon@nrao.edu, bemonts@nrao.edu

²School of Engineering and Applied Science, University of Virginia, 351 McCormick Rd, Charlottesville, VA 22904, USA

31 August 2020

ABSTRACT

X-shaped radio galaxies (XRGs) constitute a small fraction of known radio galaxies that appear to have two sets of radio jets instead of one. One proposed explanation for these double lobes is that they are relic emissions of a previous jet orientation, as might occur in the case of merging binary supermassive black holes (SMBHs). We study a large population of 131 known and candidate XRGs and identify those demonstrating clear X-shaped morphology and spectral indicators of hosting binary SMBH. 39 of the candidates were identified as XRGs by displaying four distinguishable lobes in one or both of the 1.4GHz Faint Images of the Radio Sky at Twenty- centimeters (FIRST) (Becker et al. 1995) and 3GHZ Very Large Array Sky Survey (VLASS) radio cutouts. Through spectral analysis, 8 of these XRGs were found to have double peaks at the rest-frame 4958.911 Angstrom and 5006.843 Angstrom [OIII] emission lines, indicating that they potentially host binary SMBHs. Using spectral decomposition and comparing the redshifts of the double peaks, the velocity difference between the two SMBHs in each of the binary candidates was calculated. These velocity differences were found to range between 308 ± 47 km/s to 910 ± 97 km/s, with a mean of 546 km/s, median of 524 km/s, and standard deviation of 189 km/s. This study suggests a possible connection between the observed radio morphology and kinematics of binary SMBHs and provides a handful of interesting candidates for follow-up observation for confirmation of double AGNs.

1. INTRODUCTION

Nearly every galaxy hosts a supermassive black hole at its center, and when this black hole is accreting, the active galactic nucleus (AGN) can in some cases be identifiable by the presence of two radio jets. A small fraction of these galaxies has an extra set of dimmer radio jets, the wings, which, in combination with the primary lobes, form an X-shape. Propositions to explain these X-

shaped radio galaxies (XRGs) include the relic emissions model, in which the second set of wings are relic emissions from a previous jet orientation, the hydrodynamical backflow model, in which a steep pressure gradient of ambient gas causes the backflow of electrons from the ends of the radio jets to form the smaller wings, and the superimposed twin jets proposition, in which the second set of wings is actually from a separate AGN, superimposed to look like a single structure.

The relic emissions model requires a change in jet direction, which can occur in a binary system when two SMBHs closely interact. The kinematics of two binary SMBH with AGN emission lines causes a split of the spectral line due to their relative motion. Thus, searching for XRGs that follow this relic emissions model is one way of looking for binary SMBH candidates. Therefore, in this research, we select a sample of XRGs with double peak narrow emission lines from AGN and decompose their spectra, in order to find potential candidates of XRGs hosting binary SMBH.

2. METHODS

2.1 Selecting Candidates

In identifying candidates hosting binary SMBHs, an initial pool of 131 X-shape radio galaxies compiled by Teddy Cheung (Cheung 2007 and private communication) in Table 1 was considered. They were selected firstly by their radio morphology and secondly by the shape of their radio spectra. As was available, radio image cutouts from the Karl G. Jansky Very Large Array's (VLA's) Faint Images of the Radio Sky at Twenty-one centimeters (FIRST) (Becker et al. 1995) and the Very Large Array Sky Survey (VLASS) (Lacy et al. 2020) were retrieved for each galaxy and analyzed to determine if they revealed viable XRG candidates for further analysis.

The principal criteria for narrowing down the list according to X-shaped radio morphology was the presence of 4 identifiable structures, two lobes and two wings, in both surveys. However, in the specific cases that a galaxy was especially bright or had especially large wings, it was accepted with all four features visible only in one of the two surveys. This was due to the fact that longer exposure

time could allow for better images of galaxies with wings large enough but too dim to identify and higher resolution could allow for better images of galaxies bright enough to see in their entirety but too small to distinguish two lobes and two wings. The lobes were identified as the brightest pair of diagonal features, the wings thus being the dimmer diagonal pair.

The lengths of these features were measured by an online pixel ruler on [rapidtables.com](https://www.rapidtables.com), for a comparison of lobe and wing length in each. To measure these ratios, a screenshot of the radio image was uploaded to <https://www.rapidtables.com/web/tools/pixel-ruler.html>, where one endpoint of the measurement was selected as the center of the galaxy, according to the galaxy's optical image. Then, the other endpoint was dragged around the edge of one lobe, while the pixel distance between endpoints was displayed, until the point of maximum distance was located and the distance was recorded. Then, keeping the central endpoint the same, the other end point was brought to each of the other lobes and wings and measured at the maximum distance in the same way. Fig. 1 shows how this was done for one of the galaxies, with the endpoints shown as each end of the diagonal of a rectangle. Because these measurements were in pixel count, they did not give the distance of the actual lobes and wings, but the measurements were sufficient for calculating the ratios of lobes to wings in each.

Then, of the candidates selected by morphology, the spectral data of each were acquired from the Sloan Digital Sky Survey (SDSS) (Ahumada et al. 2020) or Cheung et al. (2009) to be narrowed down further to a list only of XRGs potentially hosting binary SMBHs. The criteria for this selection was the

presence of double peaks at the two [OIII] emission lines of rest-frame wavelengths 4958.911 Angstrom and 5006.843 Angstrom, shifted according to the galaxy's redshift.

2.2 Decomposing AGN Emission Line Spectra

The spectral data of the binary XRG candidates was decomposed into multiple components for further analysis, using a combination of python and gnuplot. First, the continuum fit was found for each on python using `specutils`, an `astropy` package for spectral analysis, by their `fit_generic_continuum` function. Then, the continuum fit was subtracted from the spectral data and the resulting data was exported to an ASCII-format data file for analysis on gnuplot. On gnuplot, Gaussians were fit as appropriate around the H β , H α , and [OIII] emission line regions by the following process.

First, using the known galaxy redshift from SDSS or (Cheung et al. 2009), the emission wavelength was predicted. Second, the surrounding region (e.g., the wavelength range covering 150-250 Angstrom) was plotted. Third, as many initial Gaussian functions as necessary were defined, as $g_1(x)$, $g_2(x)$, ..., $g_n(x)$, with initial parameters estimated from visual inspection of the spectrum. Fourth, the Gaussian `fit` function was applied to each individual Gaussian, with the window of data for the fit limited to only the wavelength range of that specific Gaussian and excluding the rest of the data. If the resulting fits were not located where they should be, the initial guesses of step three were changed accordingly and step four was repeated using a modified window as necessary. Fifth, a new function, $h(x)$, was

defined as the sum of the component Gaussians, and was fit over the entire plotted region. Sixth, the result of the $h(x)$ fit was taken and modified by hand, by visually comparing with the plot. Seventh, $h(x)$ was refitted. Eighth, steps six and seven were repeated until the reduced chi squared value of $h(x)$ could not be decreased any further, indicating the best possible fit.

Finally, using python, the spectral data, continuum fit, and Gaussian components were all plotted on one set of axes. The fitting procedure is illustrated in the flow chart in Fig. 2.

2.3 Calculating Velocity Differences

With the parameters of the decomposed [OIII] double Gaussians, the velocity difference between the two AGNs could be determined based upon the difference between the mean wavelengths of each Gaussian as follows. The relationship between the speed of light, c , the source velocity, v , and redshift, z , is given by Equation (1),

$$v = cz \quad (1)$$

The definition of redshift according to observed wavelength, λ_{obs} , and rest wavelength, λ_{rest} , is given by Eq. (2),

$$1 + z = \lambda_{\text{obs}} / \lambda_{\text{rest}} \quad (2)$$

By solving Eq. (2) for z , and substituting that into Eq. (1), the formula for velocity difference according to the observed wavelength difference $\lambda_2 - \lambda_1$ was found,

$$v_2 - v_1 = (\lambda_2 - \lambda_1) * c / \lambda_{\text{rest}} \quad (3)$$

2.4 Calculating Redshift Differences

Where there was a difference between the emission line wavelength predicted by the

galaxy's redshift, and the peak in the H α and/or H β fits that correspond to the AGN, this was used to predict a possible difference between the AGN and galaxy redshift. The H α and H β emissions measured by SDSS result mostly from the AGN, due to the small aperture size used in this survey, pointed to the central region of the galaxy where the AGN dominates. For this reason, the wavelengths, λ_{obs} , corresponding to the peak of the H α and H β Gaussian fits (the means) were used to determine the AGN redshift, z_{AGN} , according to the modified version of Eq. (2) given by Eq. (4)

$$z_{\text{AGN}} = \lambda_{\text{obs}} / \lambda_{\text{rest}} - 1 \quad (4)$$

Then, this calculated z_{AGN} could be subtracted from the galaxy z value given by the SDSS to determine the redshift difference.

3. RADIO MORPHOLOGY

Narrowing down the initial list of known and candidate XRGs by their morphology resulted in a list of 39 top XRG candidates. Fig. 3 shows images of these 39 XRG candidates along with their FIRST and VLASS images, formatted on ds9 to a logarithmic power scale with contour lines at constant intervals to more clearly show their distinct lobes and wings. Fig. 3 also shows an optical r-band image of each galaxy from the Dark Energy Camera Legacy Survey (DECaLS) with the FIRST contours overlaid, to show the jets with reference to the galaxy size.

The newly released VLASS radio images were at a higher resolution (2.5 arcsec) than the FIRST images (5 arcsec), allowing for the shape of the lobes and wings to be distinguished more clearly, particularly for the small but bright galaxies. This was most

notably the case for J0220-0156, J1043+3131, J1206+0406, J1327-0203, J1614+2817, and J1323+4115, all of which did not clearly meet the criteria of having 4 distinguishable features (two lobes and two wings) by the FIRST images alone.

However, for some of the fainter radio galaxies, the VLASS image did not provide much information, and sometimes only showed small parts of the galaxies. This was true for J0115-0000, J0725+5835, J1018+2914, J1040+5056, J1130+0058, and J1202+4915, all having visible wings in FIRST but not VLASS. This can be attributed to the fact that VLASS was at a higher frequency than FIRST, and synchrotron emissions fade faster at higher frequencies than lower frequencies. A second likely cause for the decreased visibility may be the fact that at the VLASS higher resolution the sensitivity for recovering extended continuum emission is likely reduced.

The lobe to wing ratios of the list of 39 candidate XRGs are distributed as shown in the histogram in Fig. 4. The lobe to wing ratio is defined here as (the sum of the length of the lobes)/(the sum of the length of the wings) for each XRG. The length of the lobe or wing is defined as the distance from the center of the optical galaxy, to the furthest point on the outermost radio contour line of that lobe or wing, using the DECaLS images with FIRST contours from Fig. 3; except, for J1043+3131 and J1102+0250, the FIRST contours did not clearly enough distinguish the wings so the VLASS contours were used instead.

The most frequent lobe to wing ratio was between 1.30-1.40, with the majority of the galaxies having a lobe to wing ratio greater than one. However, 5 of the galaxies did have

a ratio less than one, indicating their wings appeared longer than their lobes.

4. SPECTRAL ANALYSIS

4.1 Decomposed Spectra

There were 8 of the X-shaped morphology candidates that showed the double peaked [OIII] emission lines. Fig. 5 shows these 8 binary XRGs along with their entire spectra in the top left for each XRG, featuring the observed spectrum in blue, the continuum fit overlaid in orange, as well as vertical lines on the predicted wavelengths of several notable emission lines, according to the galaxy's redshift. From left to right those spectral emission lines represent [OII] in purple, H β in yellow, [OIII] in green, [NII] in blue, H α in red, and [NII] in blue.

The gnuplot Gaussian fit process was done for the [OIII] regions of each of the 8 binary candidates, with the resulting parameters in Table 2 and decomposed spectra in the bottom left for each XRG in Fig. 4. For each candidate, a double Gaussian fit was able to be applied to both [OIII] emission lines, except for J0220-0156 and J1600+2058 which only allowed for a single Gaussian fit for the [OIII] emission at 4959 angstrom, likely due to noise and/or blending, but still a double Gaussian for the [OIII] emission at 5007 angstrom. The peaks of [OIII] emission line at 5007 angstrom were more than twice the amplitude of the peaks of [OIII] emission line at 4959 angstrom. Furthermore, for every double Gaussian one peak was notably higher than the other, and whether this was the redshifted or blue-shifted peak was consistent for both [OIII] emissions within each individual XRG plot, but not consistent across all the plots.

The standard deviations of most of the Gaussians were similar, ranging between 3-6 Angstrom with the following exceptions: The single Gaussian in J1600+2058 was particularly wide with a standard deviation of 10.20 Angstrom, which may be a result of severely blended double peaks, and J0220-0156 had one component of the double Gaussian being very narrow with a mere 1.02 Angstrom standard deviation, which combined with the fact that the other emission line was only a single Gaussian, raises the possibility that this is not a true double peak. J0941+3944 also had more narrow peaks ranging from 2.00-2.17 Angstrom, but this is not particularly notable because they are nearly the same for each component. Conversely, J0914+1715 was interesting in that the blue-shifted components of both emission lines, 3.03 and 2.41 Angstrom, were significantly narrower than the right components of 5.17 and 6.89 Angstrom.

Following the [OIII] plot, the H α and H β regions were also decomposed and plotted, as allowed by the data available, noting that many of the galaxies with higher redshifts did not have data in the H α region. Table 2 gives the resulting parameters and the top right and bottom right for each XRG in Fig. 4 show the decomposed H β and H α plots, respectively, that were available for these 8 binary XRGs.

Every XRG had a sufficient signal-to-noise ratio (S/N) of an H β emission for a Gaussian fit to be possible, but the S/N was only marginal for J0220-0156, J0941+3944, and J1430+5217. The H β peak was almost indistinguishable from noise for J0917+0523, J1406-0154, and J1600+2058. There was only one Gaussian component for the majority of the H β fits, with the exceptions of J0914+1715 with a broad and narrow line, and J0941+3944 with two peaks that were too small to clearly

categorize but appeared to be narrow. These two double Gaussians were distinguishable because they were shifted slightly apart, but the others may have also had multiple components that would not have been distinguishable without a wavelength shift between them.

Only J0220-0156, J0914+1715, J0941+3944, and J1600+2058 had any H α data, but these all had clear narrow Gaussian peaks at H α as well as a distinguishable [NII] peak to the right. J0220-0156 and J1600+2058 also had broad H α Gaussians blue-shifted with respect to the other narrow emission line components. J0941+3944 was interesting in that it appeared to have two narrow H α components, as well as an [NII] peak to the left. J0914+1715 had too much noise to distinguish anything beyond the aforementioned H α and [NII] peaks that were visible in all the plots.

4.2 Velocity Differences

Table 3 lists the velocity differences ($v_2 - v_1$) determined by Eq. (3) for each predicted Binary XRG. For each of the XRGs that it was possible to fit double Gaussians to both [OIII] emission lines the velocity difference was calculated as the average of the two. The range of velocity differences varied from 308 ± 47 km/s to 910 ± 97 km/s, with a mean of 546 km/s, median of 524 km/s, and standard deviation of 189 km/s.

4.3 Redshift Differences and AGN Velocities

Several of the spectral plots had the emission data shifted slightly from the emission lines predicted by the SDSS

redshifts. This shifted data indicated a difference in redshift, ($z - z_{\text{AGN}}$), between the AGN and the galaxy. These redshift differences were calculated by determining z_{AGN} according to each H β and H α Gaussian fit and retrieving z from the SDSS, with the results shown in Table 4. Table 4 also lists the velocities of the AGN relative to their galaxies, v_{AGN} , corresponding to each redshift difference. There is no z , ($z - z_{\text{AGN}}$), v_{AGN} listed for J0220-0156 because this galaxy did not have spectral data in the SDSS database, so the redshift used for its emission lines was instead the AGN redshift acquired from (Cheung 2009).

This shift between the AGN data and galaxy emission line was apparent in the [OIII] plots when the galaxy emission line was not centered between the double peaks of the [OIII] emissions, such that the galaxy emission line was red or blue-shifted from the dip between the double peaks. This was the case for J0914+1715, J0917+0523, J1406-0154, and J1430+2058.

J0917+0523 had no H α data, but the H β shift visually matched the [OIII] shifts, with a redshift difference of -0.000498 ± 0.000351 and AGN velocity of $4,080 \text{ km/s} \pm 106,638 \text{ km/s}$. Similarly, J1406-0154 had no H α data, but the H β visually matched the [OIII] shifts, with a redshift difference of -0.000937 ± 0.000441 and AGN velocity of $147,697 \pm 132,240$. This was also the case for J1430+5217 in which there was no H α data but the H β shift visually matched the [OIII] shifts, with a redshift difference of -0.000336 ± 0.000079 and AGN velocity of 10310 ± 23681 .

The H α shift appeared similar to that in the [OIII] plot for J0914+1715, but was not supported by the H β plot where the narrow

component seemed to be shifted in the opposite direction. The rest of the binary XRG candidates did not have data shifts that matched between their H β , [OIII], and H α plots.

5. DISCUSSION

5.1 Morphology

Typically, the wings of an XRG are expected to be shorter than the lobes, and this was the case for the majority of the XRG candidates analyzed as shown in Fig. 2. However, the five that had longer wings than lobes can be understood by considering their orientation, with the lobes being less perpendicular than the wings to the line of sight.

5.2 Understanding AGN Signatures

For AGN, there are expected to be a broad and narrow component for the H α and H β emission lines, with the broad component coming from the fast-moving hydrogen gas nearest the nucleus and the narrow component coming from the slower orbiting gas further from the nucleus. However, for the XRGs, the clearest visibility of the radio jets requires that the rotation axis be roughly orthogonal to the line of sight and that the accretion disk be parallel to the line of sight. At this orientation the dust torus surrounding the accretion disk blocks the broad line emissions, explaining why there are only narrow emissions for several galaxies. However, for all the H β emissions the S/N was too low to clearly distinguish if there were both broad and narrow line components or not.

For the H α emissions, it was possible to distinguish a broad line emission separate

from the narrow line emission when this broad emission was blue-shifted, as was the case for J0220-0156 and J1600+2058. A shift in the broad emission line can be explained by a gravitational wave occurring, resulting in a directional kickback for the AGN and broad emission line region. However, given that the S/N of the broad emission line was not very strong for most of the XRG samples in this study, detailed investigation and modeling work is required to make a definitive conclusion.

The shifts in narrow emission line data from the predicted SDSS emission lines, and thus differences in AGN and galaxy redshifts, were also found. While this shift was apparent based on the H β plots for J0917+0523, J1406-0154, and J1430+5217, the error on each of their calculated redshift differences was to the same order of the magnitude as the redshift difference, making these results inconclusive. The precision of the results for these three galaxies specifically could be improved by acquiring H α data, such that an average of the two emission line results could be calculated. A higher S/N would be necessary to decrease the error in the fit parameters and resulting redshift differences, and thus provide more conclusive results. Further investigation, verifying the redshifts that were associated with the galaxies, is also necessary to make a definite conclusion about the galaxy vs. AGN redshift differences.

5.3 Implications of Binary Signatures

The double peaks of the [OIII] emission plots in Fig. 4 are strong indicators that these XRGs each have two SMBHs at their center with different velocities relative to us. Another possible explanation for double peaks is the outflow scenario, in which outflowing material would have shifted emission lines due to their motion. However,

in the cases of the XRGs, for the lobes and wings to be clearly visible they must be orthogonal to our line of sight, meaning the outflowing material would move mostly perpendicular to our line of sight causing no visible difference in velocity. This leaves binary SMBHs as the most likely explanation for the double [OIII] peaks. A ramification of these XRG's hosting binary SMBHs is that the strong gravitational interaction between these two bounded SMBHs would cause a change in spin.

A significant reorientation of the jet axis requires strong interaction between the SMBHs, as is the case when there is a small separation between the SMBHs. Due to conservation of angular momentum, a small separation correlates to a high radial velocity, for which the measured velocity differences serve as an indicator. However, because the calculated velocity differences only consider the component of each AGN velocity parallel to the line of sight, any velocity difference component perpendicular to our line of sight would indicate a higher true velocity difference of the AGN. Therefore, each calculated difference should be considered as the minimum velocity difference between those two AGN. The velocity differences measured do indicate a likelihood that the kinematics of the binary SMBHs would allow for a significant reorientation, as they all had an order of magnitude of 100 km/s, meaning a true velocity difference on the order of 100 km/s or higher.

This jet reorientation is the primary qualification for the relic emissions model, thus offering strong evidence that the binary XRG candidates' wings are relic emissions from a previous jet orientation.

Not only do these results support the relic emissions model as an explanation for the occurrence of XRGs, but they also offer a new way of searching for binary SMBHs. The class of XRGs following the relics emissions model, identifiable by a combination of radio imaging and optical spectral analysis, serves as a pool of candidates within which SMBHs can be searched.

6. FUTURE GOALS

The next primary goal is to confirm two AGNs in these binary SMBH candidates, using higher resolution radio imaging. My advisors and I proposed VLBA observation of one of our candidates to confirm its dual AGN in the center. With these observations it should be possible to locate the AGN in X-band and detect extended radio jet emission in S-band. And, also using the [OIII] emission luminosity, we intend to estimate the accretion rate and SMBH mass of these AGN.

Another goal is to study the dynamics of the binary SMBHs further, as developing a clearer understanding of the AGN kinematics may offer further support for the relic emissions theory. While the velocity differences serve as a strong indicator of merging SMBHs, they do not tell the whole story, leaving unanswered the questions of separation and orbital velocity. It is possible to estimate the separation of the two SMBHs by supplementing the velocity difference results with an assumption of orbital configuration and the SMBH masses.

Finally, further evidence for the relic emissions theory may come from study of the radio spectral index of the wings and lobes, as the spectral energy distribution (SED) of the radio emissions becomes steeper with time.

Our recent 10GHz VLA observation (VLA/20A-459) combined with the existing 1.4 and 3GHz images with similar resolution can allow for a study of the radio SED of lobes and wings to infer the age of radio emission. Past studies using this model have indicated higher steepness in the wings, and verification of this with more data at various frequencies would provide evidence for the wings being older and likely relic emissions.

7. CONCLUSION

To summarize, J0036+0048, J0220-0156, J0914+1715, J0917+0523, J0941+3944, J1406-0154, J1430+5217, and J1600+2058 were identified as XRGs and predicted to host binary SMBHs. The existence of binary SMBHs in XRGs supports the relic emissions model as an explanation for the second set of wings in these XRGs. Support for the prediction that these XRGs host binary SMBHs may be supported by future study and more XRGs hosting SMBHs may be found. Through this, the existence of XRGs and the behavior of merging SMBH may be further understood.

8. ACKNOWLEDGMENTS

This study would not have been possible without the guidance of my advisors, Ilsang Yoon and Bjorn Emonts. Support for this study came from the Research Experiences for Undergraduates program of the National Science Foundation and the National Radio Astronomy Observatory. The National Radio Astronomy Observatory is a facility of the National Science Foundation operated under cooperative agreement by Associated Universities, Inc.

This study also utilized data from the SDSS Sky Survey. Funding for the Sloan Digital Sky Survey IV has been provided by the Alfred P. Sloan Foundation, the U.S. Department of Energy Office of Science, and the Participating Institutions. SDSS acknowledges support and resources from the Center for High-Performance Computing at the University of Utah. The SDSS web site is www.sdss.org.

SDSS is managed by the Astrophysical Research Consortium for the Participating Institutions of the SDSS Collaboration including the Brazilian Participation Group, the Carnegie Institution for Science, Carnegie Mellon University, Center for Astrophysics | Harvard & Smithsonian (CfA), the Chilean Participation Group, the French Participation Group, Instituto de Astrofísica de Canarias, The Johns Hopkins University, Kavli Institute for the Physics and Mathematics of the Universe (IPMU) / University of Tokyo, the Korean Participation Group, Lawrence Berkeley National Laboratory, Leibniz Institut für Astrophysik Potsdam (AIP), Max-Planck-Institut für Astronomie (MPIA Heidelberg), Max-Planck-Institut für Astrophysik (MPA Garching), Max-Planck-Institut für Extraterrestrische Physik (MPE), National Astronomical Observatories of China, New Mexico State University, New York University, University of Notre Dame, Observatório Nacional / MCTI, The Ohio State University, Pennsylvania State University, Shanghai Astronomical Observatory, United Kingdom Participation Group, Universidad Nacional Autónoma de México, University of Arizona, University of Colorado Boulder, University of Oxford, University of Portsmouth, University of Utah, University of Virginia, University of Washington, University of Wisconsin, Vanderbilt University, and Yale University.

REFERENCES

- Ahumada et al. 2020, ApJS, 249(1), The 16th Data Release of the Sloan Digital Sky Surveys: First Release from the APOGEE-2 Southern Survey and Full Release of eBOSS Spectra
- Becker et al. 1995, ApJ, 450, 559, The FIRST Survey: Faint Images of the Radio Sky at Twenty Centimeters
- Cheung 2007 AJ, 133, 2097, FIRST ``Winged" and X-Shaped Radio Source Candidates
- Cheung et al. 2009 ApJS 181, 548, FIRST "Winged" and X-Shaped Radio Source Candidates. II. New Redshifts
- Huang et al. 2019, AJ, 157(5), Overview of the DESI Legacy Imaging Surveys
- Lacy et al. 2020, PASP, 132(1009), 035001, The Karl G. Jansky Very Large Array Sky Survey (VLASS). Science Case and Survey Design

Table 1 Coordinates of Known and Candidate XRGs from Teddy Cheung

New or Other Examples	Known XRGs (Cheung 2007)	Sample of First Candidates (Cheung 2007)					
07 23 10.1 +32 10 03	00 09 52.6 +12 44 05	00 01 40.2 -00 33 51	08 45 08.4 +40 31 15	11 20 16.2 +43 54 51	13 09 49.7 -00 12 36	14 44 07.2 +41 47 50	
07 57 37.4 +57 39 32	00 58 22.6 +26 51 58	00 33 02.4 -01 49 57	08 46 03.6 +39 56 58	11 28 37.7 +19 19 53	13 10 15.3 +54 58 35	14 54 42.2 +27 32 12	
09 13 46.880 +35 09 02.60	02 20 54.2 -01 56 52	00 36 36.2 +00 48 53	08 59 50.2 -04 33 07	11 35 36.8 -07 37 00	13 16 38.2 +24 27 32	14 55 58.3 +32 37 33	
09 32 37.3 +16 12 02	05 16 03.1 +24 58 25	00 45 41.9 +00 21 06	09 14 05.2 +17 15 54	11 40 49.7 +10 57 56	13 27 38.2 -02 03 10	14 56 43.2 +25 42 18	
13 16 42.8 +61 55 30	08 05 29.9 +24 10 04	00 49 39.4 +00 59 54	09 17 45 +05 23 00	12 00 06.0 +61 05 45	13 30 10.3 -02 06 18	14 59 41.9 +29 03 32	
13 23 24.3 +41 15 15	08 31 21.2 +32 18 51	01 13 41.1 +01 06 09	09 24 47.0 +42 33 47	12 01 25.7 -07 03 11	13 39 34.2 -00 16 36	15 01 57.4 +07 52 27	
13 33 45.1 +02 19 12	09 41 24.0 +39 44 42	01 15 27.4 -00 00 02	09 41 22.6 -01 43 01	12 02 35.1 +49 15 32	13 42 45.3 +25 47 12	15 15 33.6 -05 32 51	
02 45 13.481 +10 47 22.80	10 20 53.7 +48 31 24	01 43 16.7 -01 19 01	09 41 58.3 +21 47 44	12 06 17.3 +38 12 35	13 45 41.6 +52 33 36	15 22 13.1 +45 27 57	
08 08 01.02 +48 38 07.1	11 01 51.900 +16 40 38.70	01 44 10.0 -08 30 03	09 43 02.2 +28 34 46	12 07 32.9 +33 52 40	13 48 04.6 +44 11 24	15 37 07.3 +26 48 23	
10 18 26.94 +29 14 21.7	11 30 21.4 +00 58 23	01 45 20.0 -01 59 48	10 05 52.5 +11 54 37	12 10 18.8 -03 41 53	13 51 42.1 +55 59 43	16 00 38.9 +20 58 52	
11 59 05.7 +58 20 36	12 06 19.902 +04 06 11.48	01 47 19.3 -08 51 20	10 08 11.4 +00 30 00	12 10 12.0 +11 21 03	13 53 06.3 +07 24 36	16 03 45.0 +52 42 21	
17 23 20.8 +34 17 58	13 57 30.6 +48 07 42	02 11 46.9 -09 20 37	10 15 41.1 +59 44 45	12 11 02.5 +45 39 14	14 06 48.6 -01 54 17	16 06 12.7 +00 00 27	
20 18 01.3 -55 39 31	15 13 40.1 +26 07 31	02 25 08.6 -07 38 49	10 40 22.5 +50 56 25	12 18 59.1 +19 55 28	14 06 02.4 +06 57 16	16 06 38.9 +45 17 36	
	18 24 33.0 +74 20 59	07 02 47.9 +50 02 05	10 43 18.6 +31 31 06	12 27 12.5 -07 42 02	14 08 28.4 +02 25 50	16 14 28.4 +28 17 31	
	19 52 15.8 +02 30 24	07 25 32.3 +58 35 27	10 49 35.3 +44 22 04	12 27 49.4 +21 55 19	14 11 21.1 +09 07 35	16 25 30.7 +27 05 46	
	21 23 44.5 +25 04 12	08 05 44.0 +48 54 58	10 54 00.8 +55 21 48	12 28 03.8 +26 42 27	14 24 40.5 +26 37 31	16 53 37.3 +31 15 28	
	21 57 31.438 +00 37 57.07	08 13 00.1 +43 47 49	10 55 52.5 -07 07 19	12 32 52.5 -07 17 29	14 30 17.3 +52 17 35	16 55 16.3 +45 51 06	
	23 47 38.1 +08 52 46	08 21 49.6 +29 22 44	11 02 06.6 +02 50 45	12 47 26.8 +46 46 06	14 33 51.9 +00 37 23	16 56 36.6 +39 52 58	
		08 36 35.4 +31 25 51	11 11 39.7 +40 50 24	12 53 24.3 +34 35 18	14 34 02.2 +59 06 53	22 26 45.6 +01 25 11	
		08 38 44.6 +32 53 12	11 14 27.1 +26 32 59	12 58 32.9 +32 27 41	14 37 38.9 +08 34 22	23 59 46.5 -10 41 15	

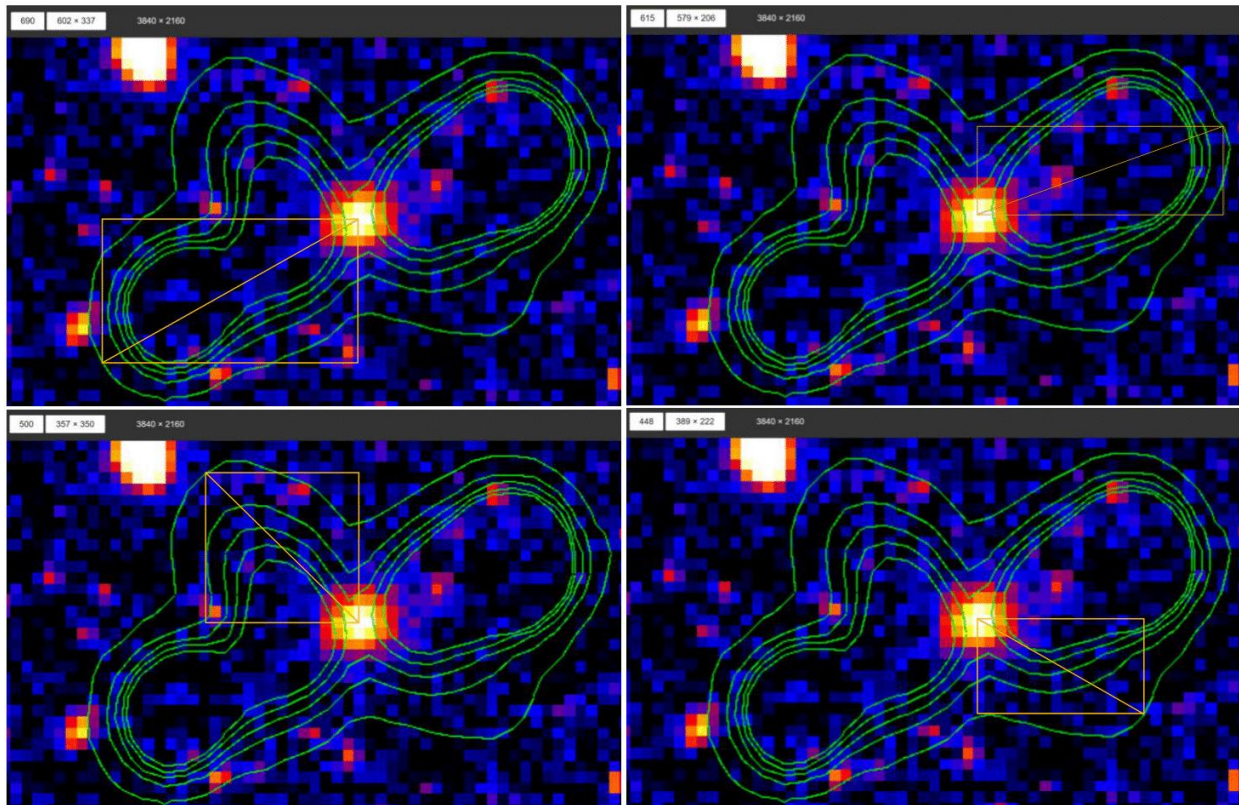


Figure 1 Example of pixel ruler being used to measure the lengths of the lobes and wings of one XRG, J0036+0048. The optical r-band emissions from DECaLS of the galaxy is shown the background of the 1.4GHz FIRST contours in green. The distance measured for each lobe and wing is shown in yellow as the diagonal of the rectangles.

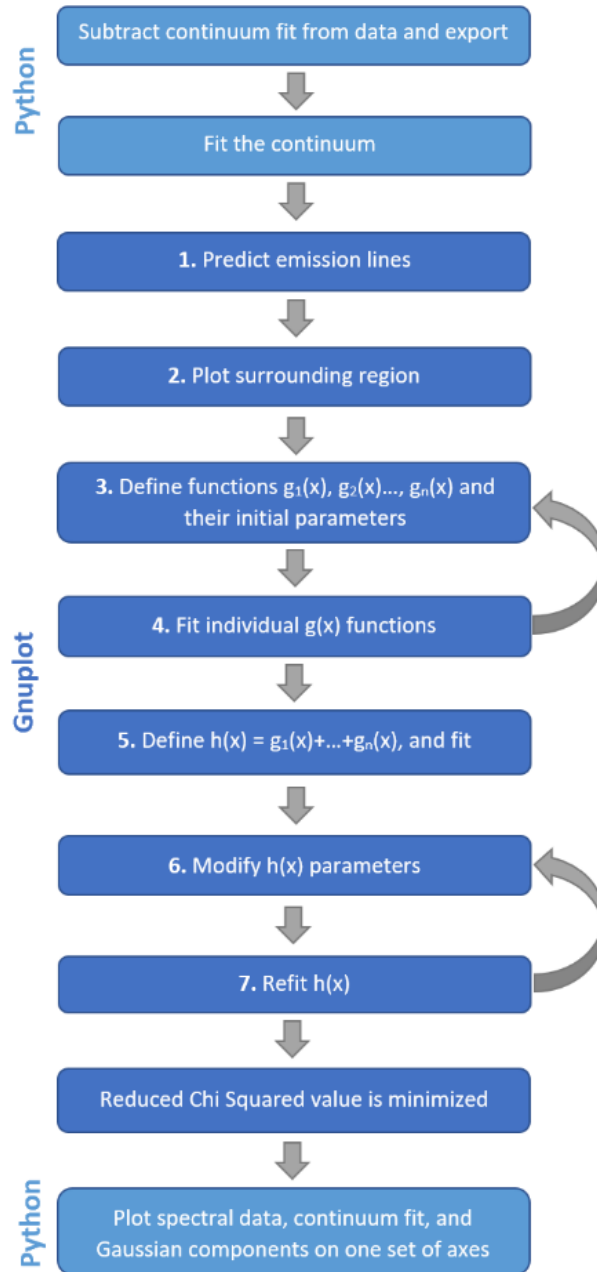
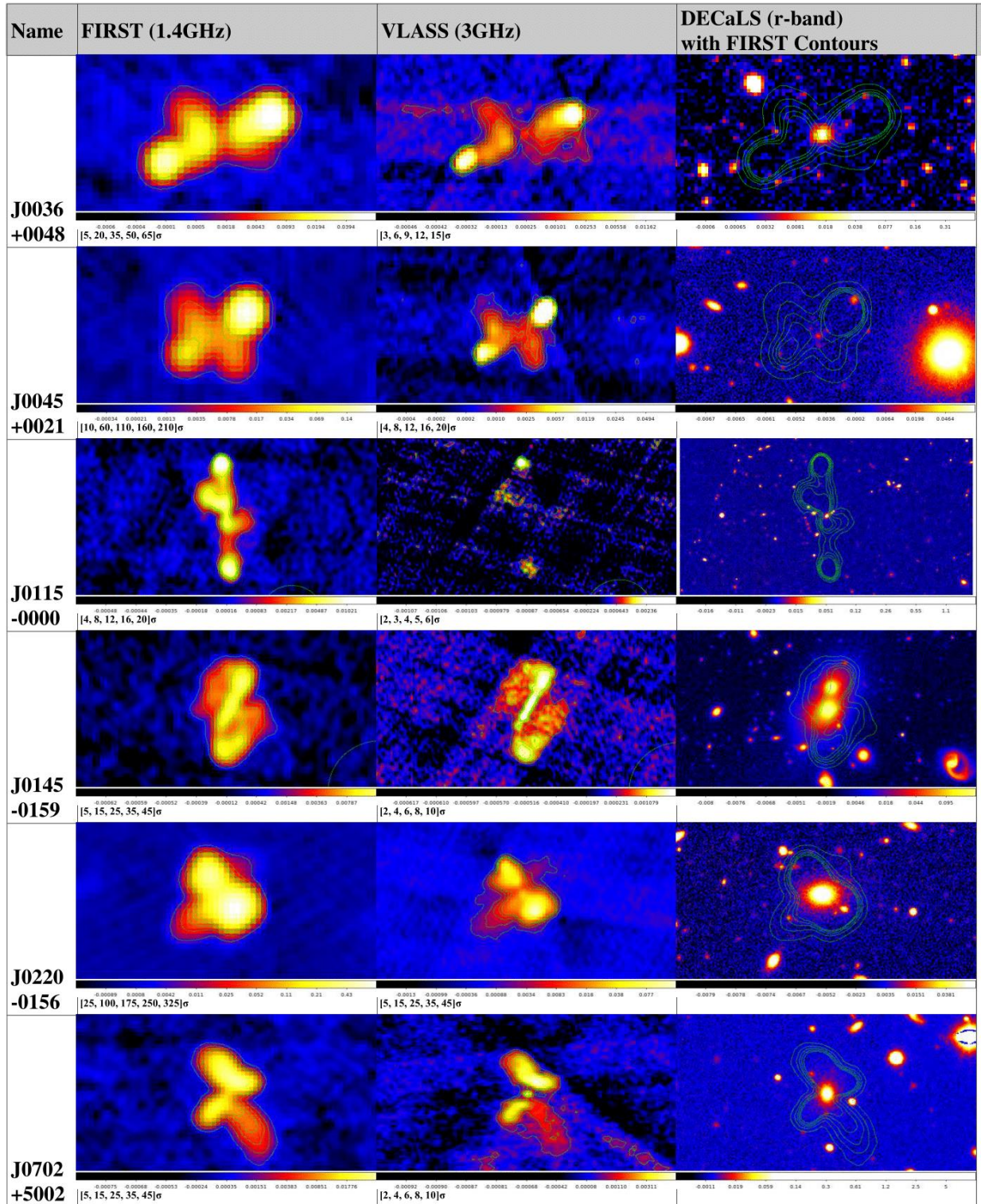
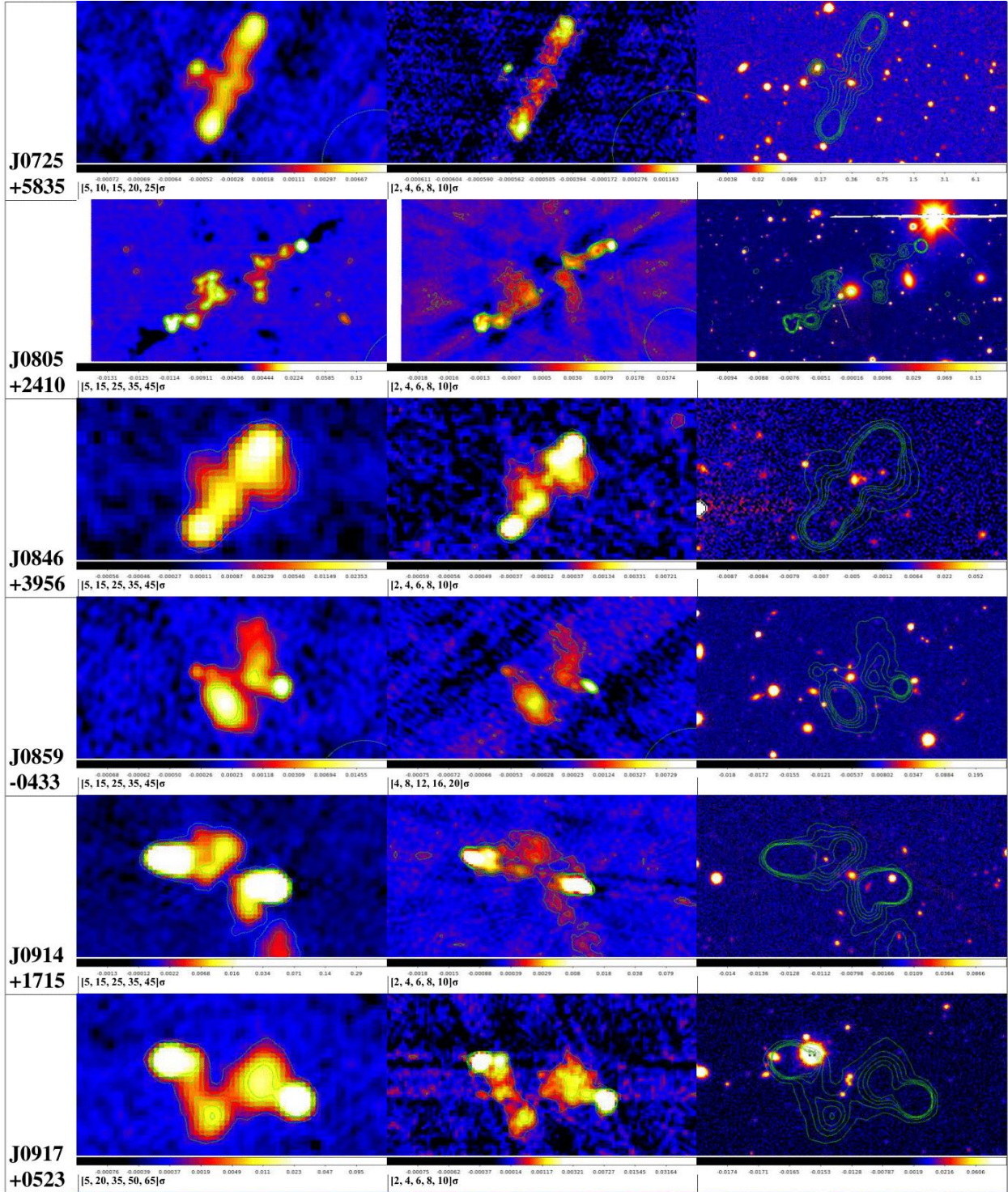
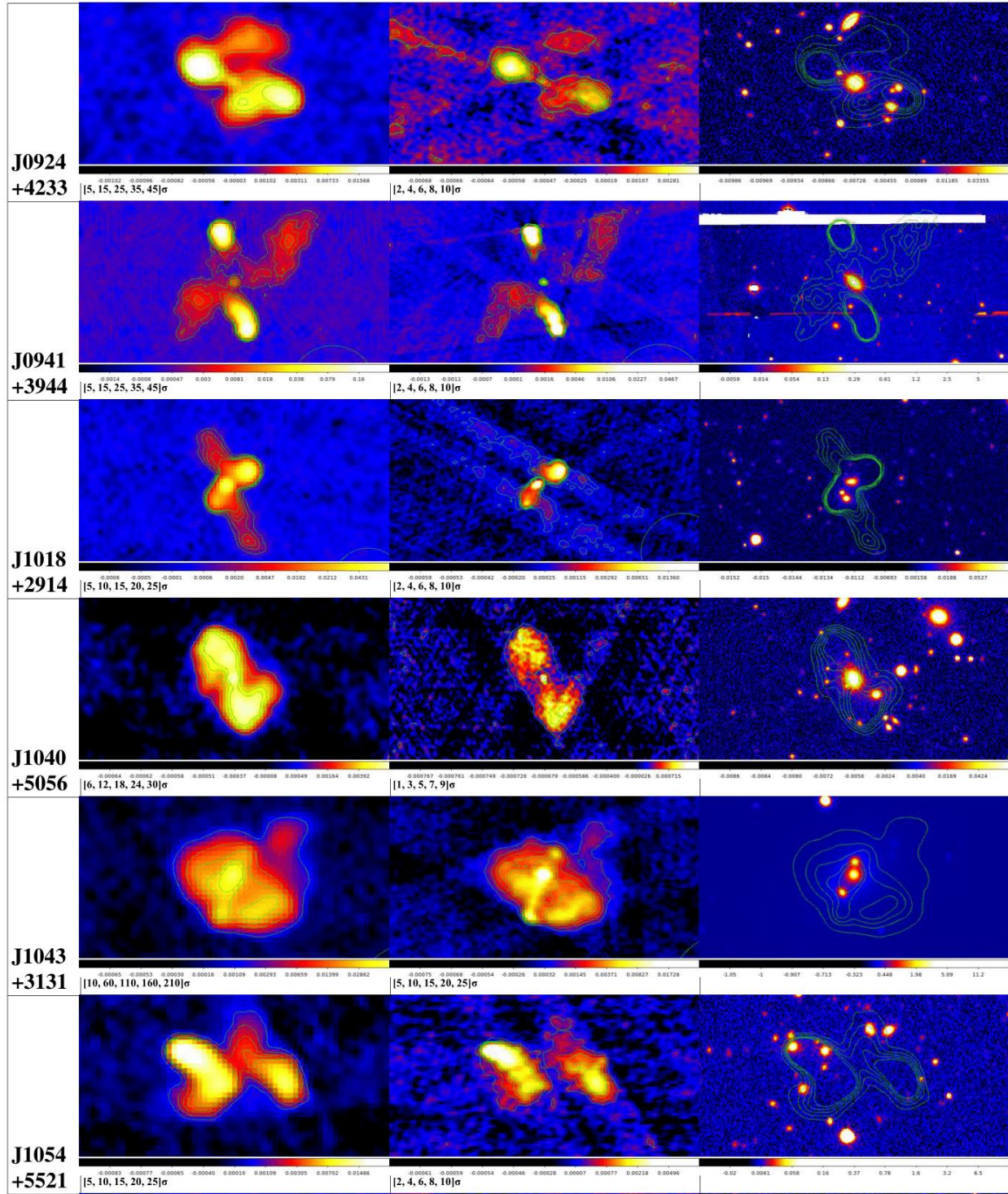


Figure 2 Flowchart of spectral decomposition process

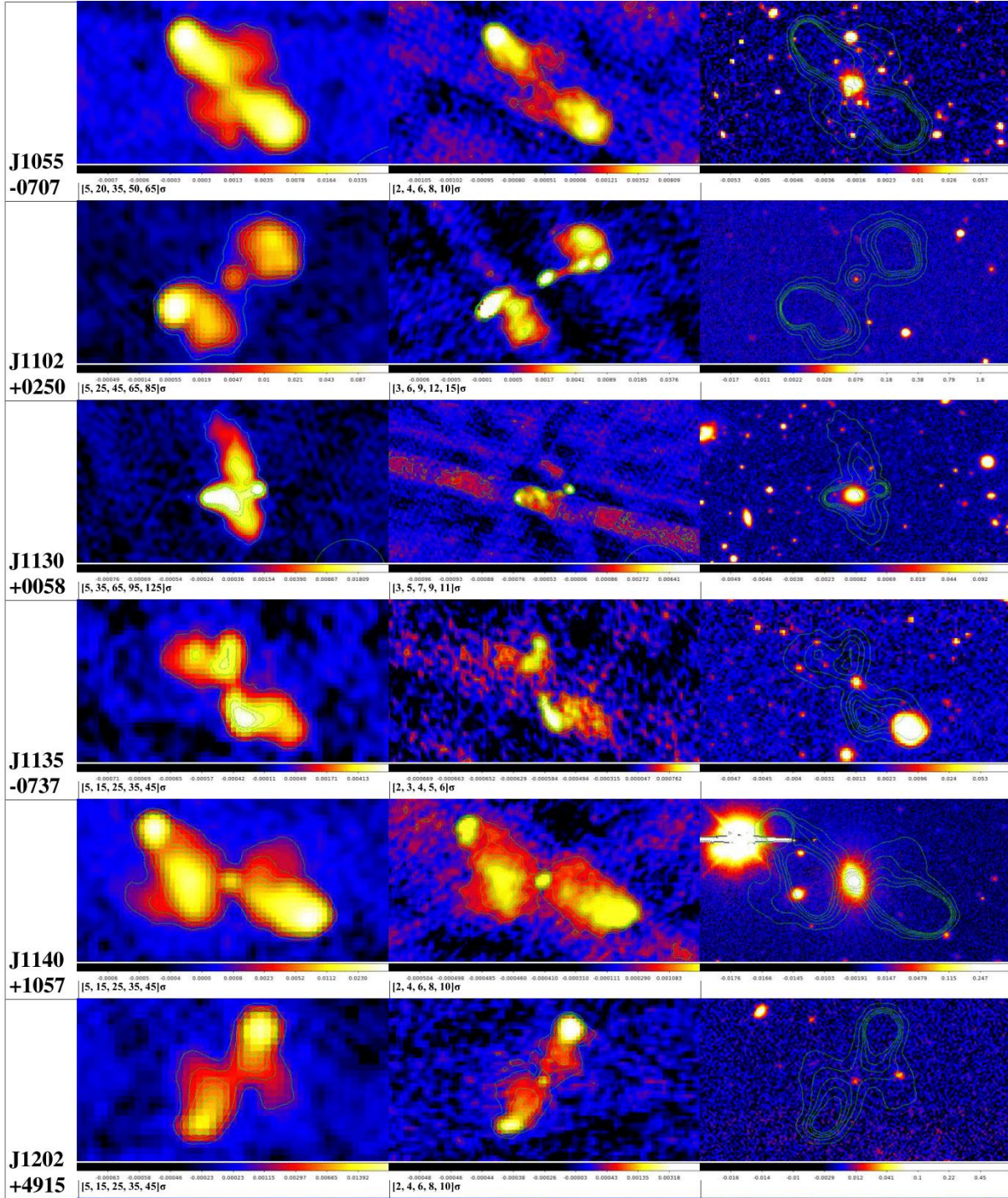


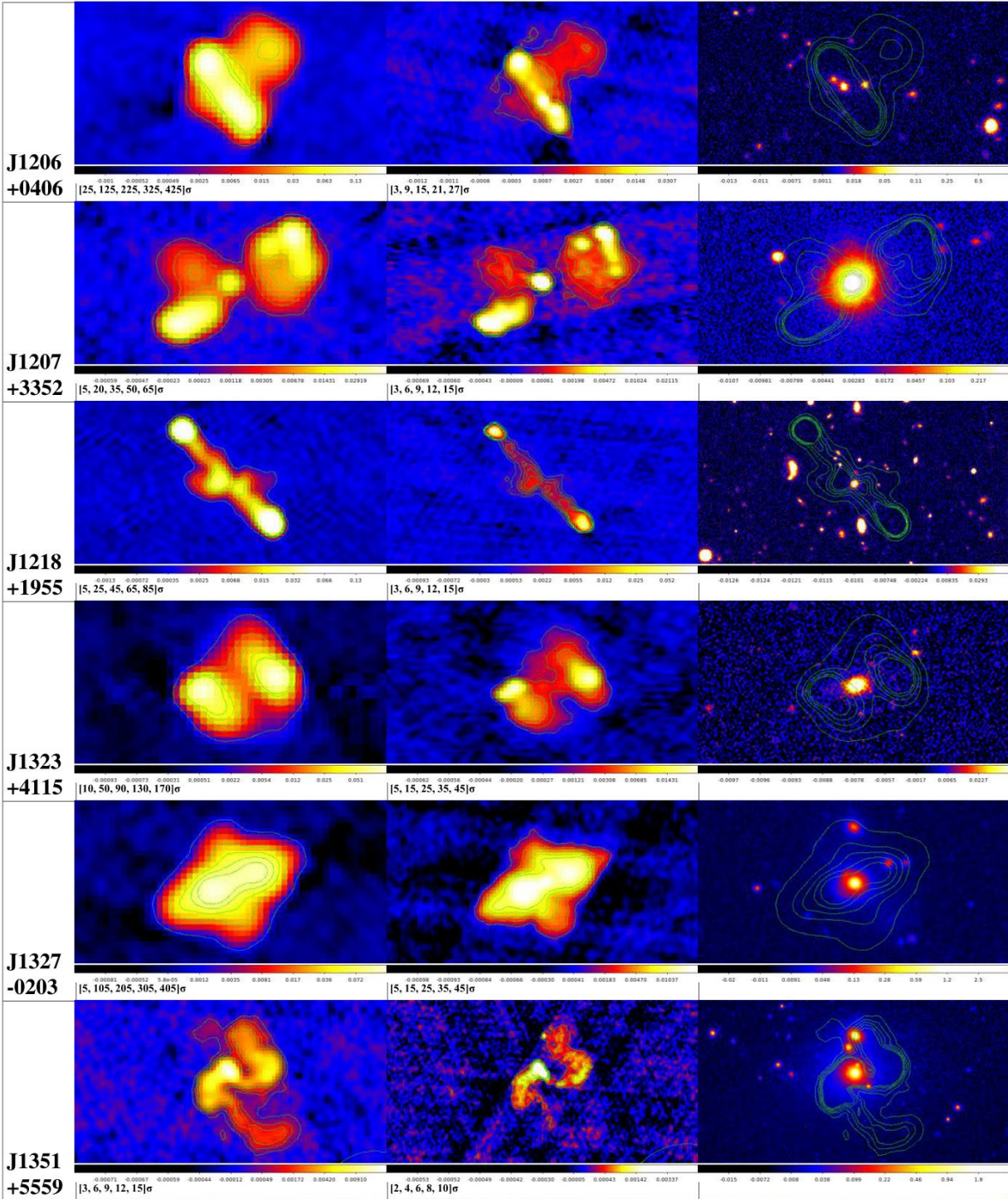
Searching for X-Shaped Galaxies Hosting Binary Supermassive Blackholes



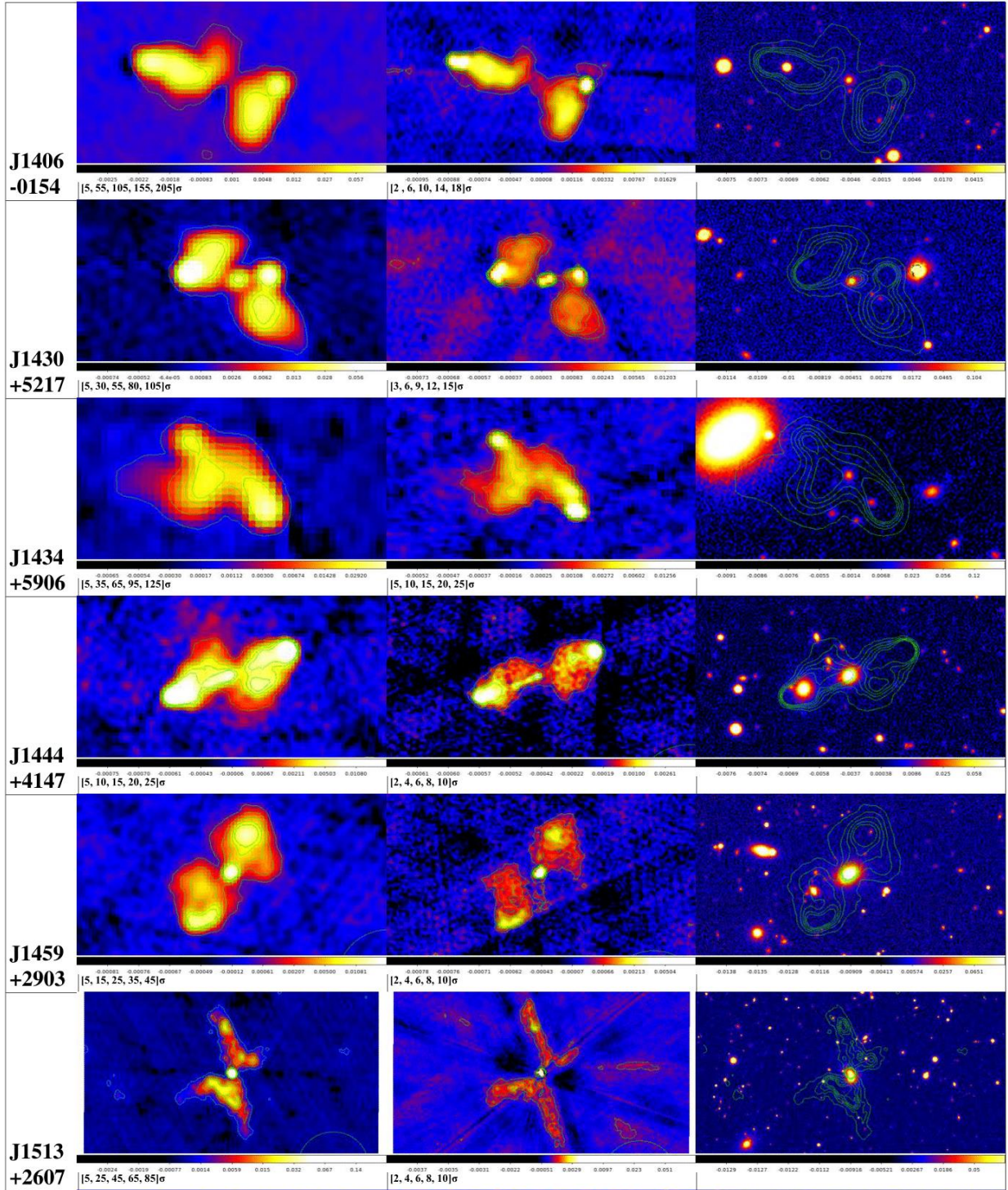


Searching for X-Shaped Galaxies Hosting Binary Supermassive Blackholes





Searching for X-Shaped Galaxies Hosting Binary Supermassive Blackholes



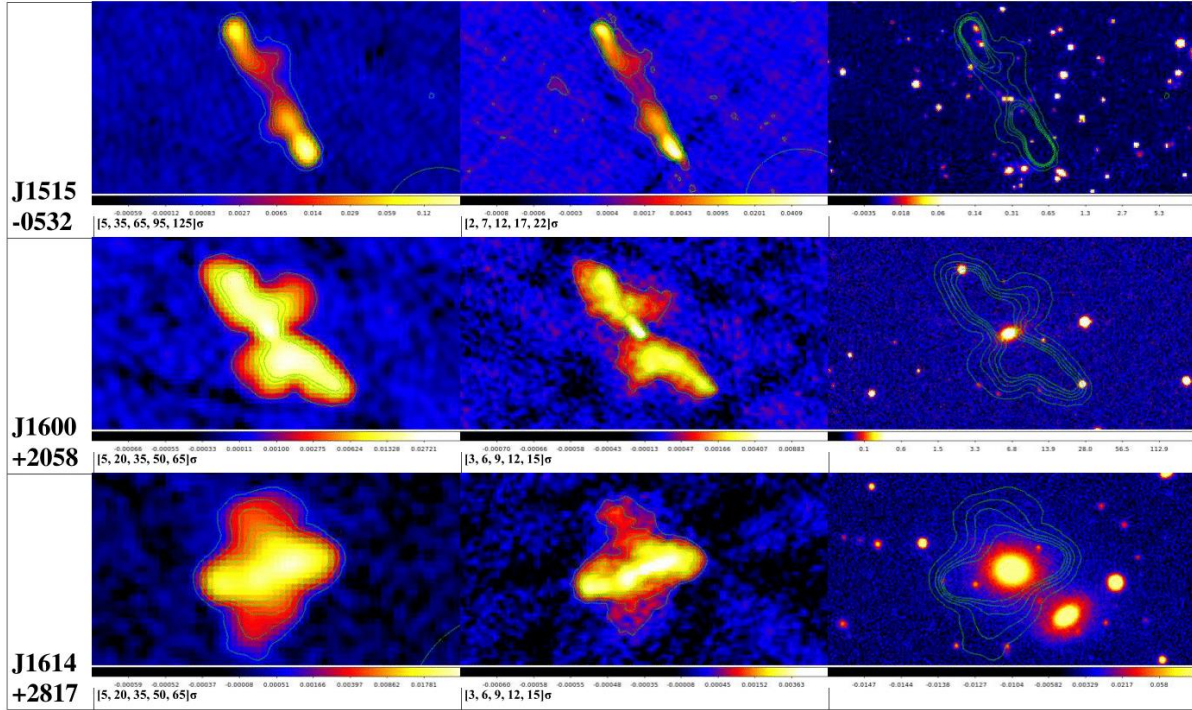


Figure 3 XRG candidates selected by their X-shape morphology. The first and fifth columns show the 1.4GHz FIRST radio emissions, the second and fifth columns show the 3GHz VLASS radio emissions, and the third and fifth columns show the DECaLS r-band optical emissions for each XRG. Underneath the FIRST and VLASS images the contour levels for each are listed.

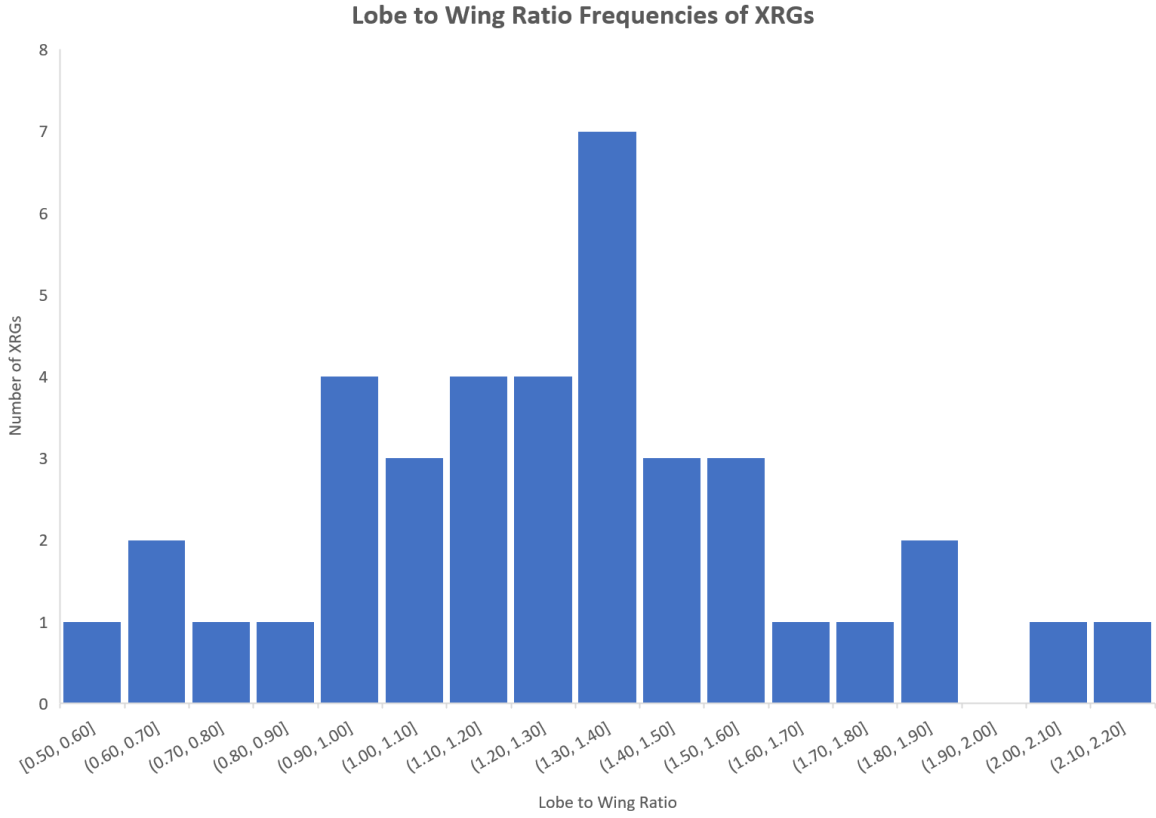
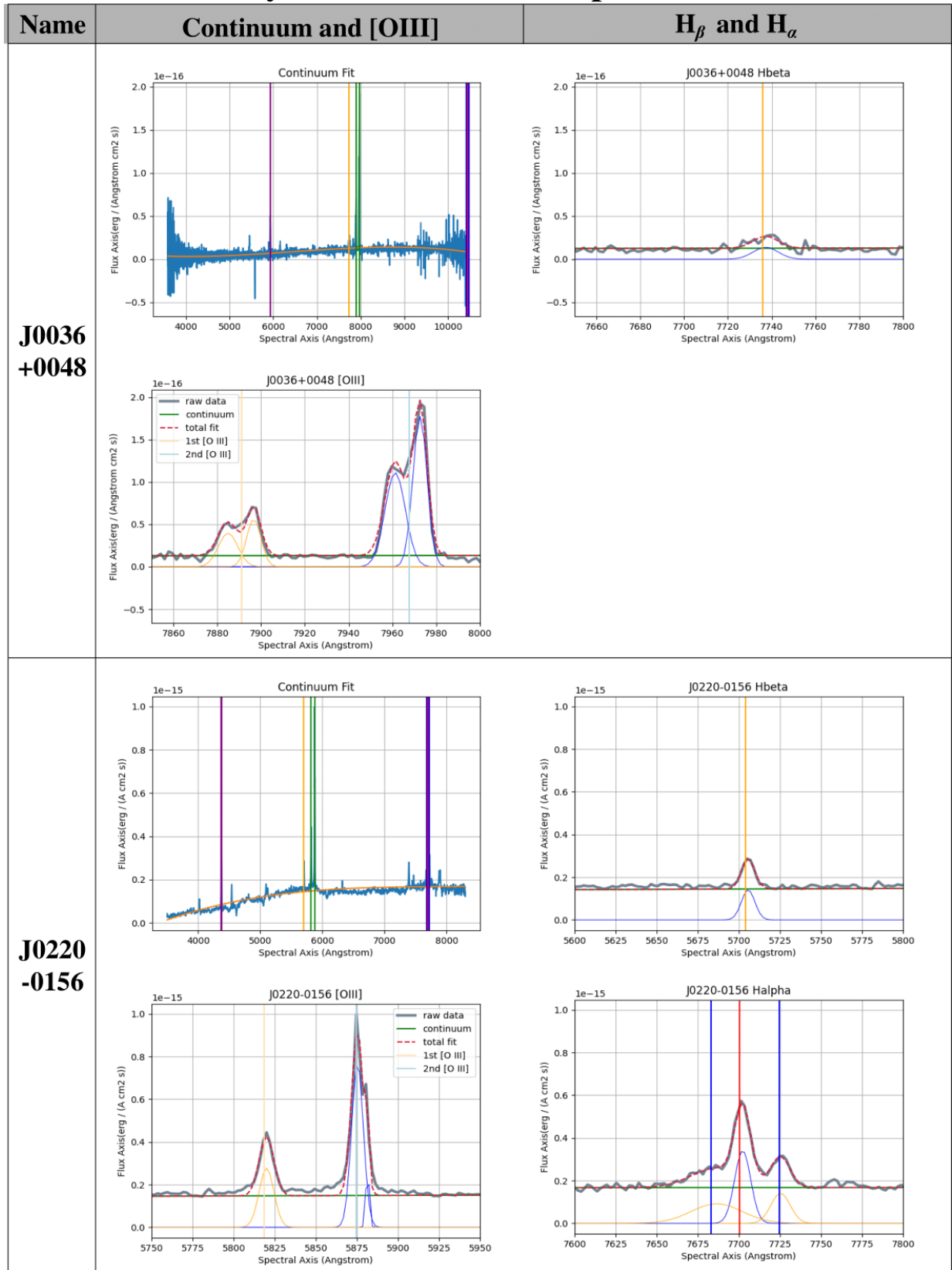


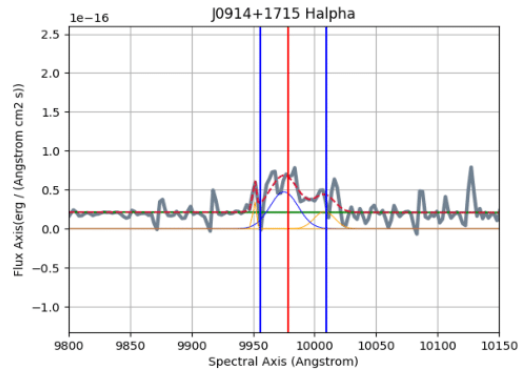
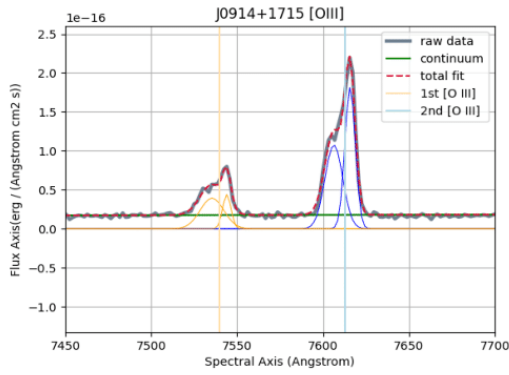
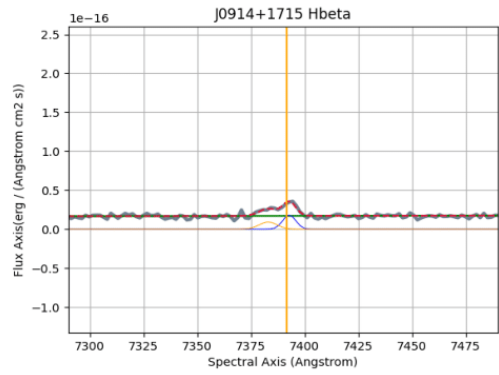
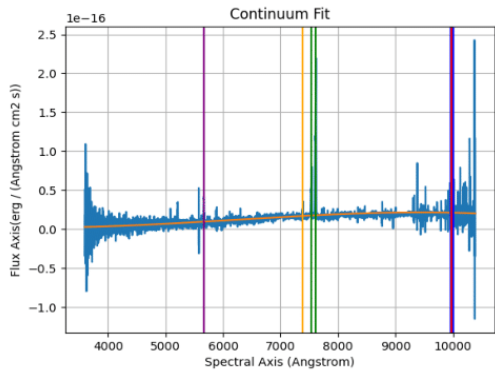
Figure 4 Histogram of the lobe to wing ratios of the XRG candidates selected by morphology

Binary XRG Candidates' Spectral Plots

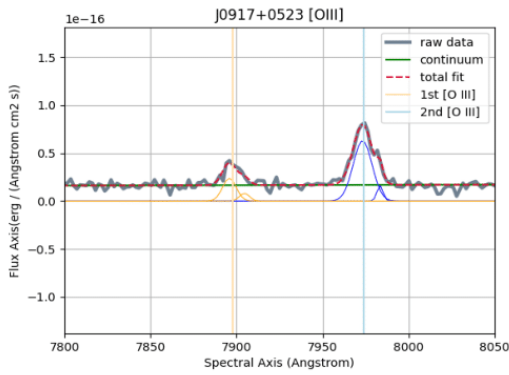
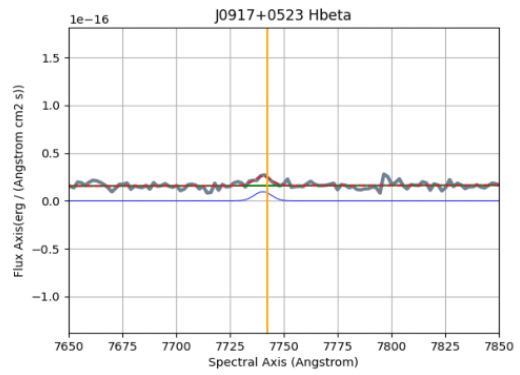
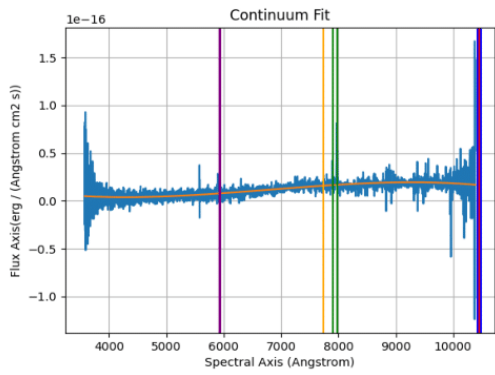


Searching for X-Shaped Galaxies Hosting Binary Supermassive Blackholes

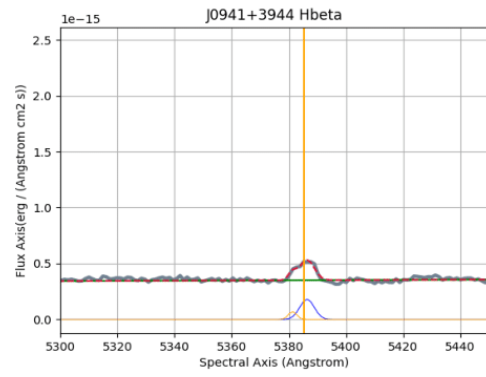
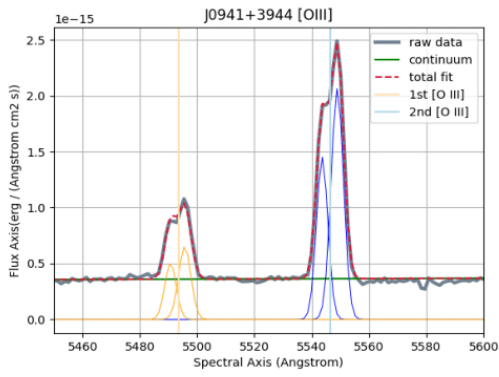
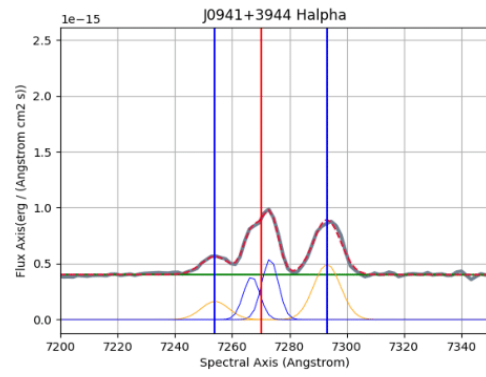
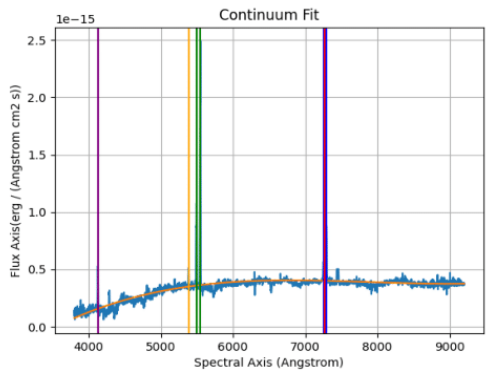
**J0914
+1715**



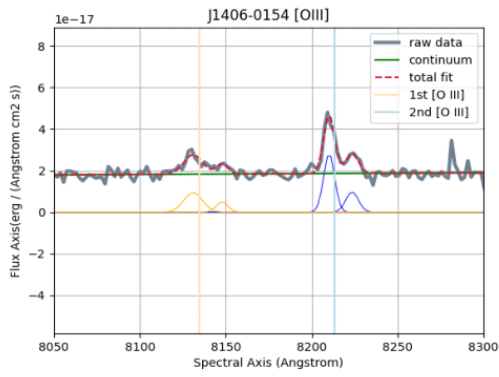
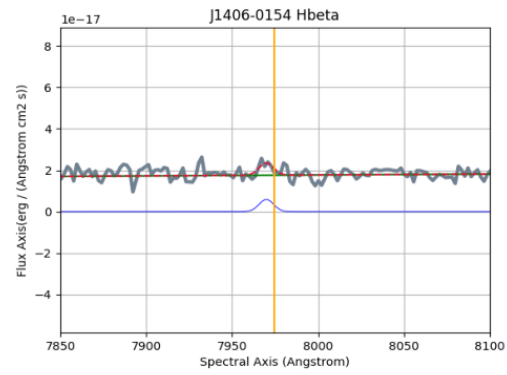
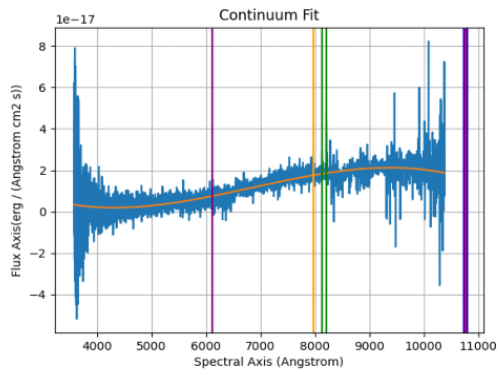
**J0917
+0523**



**J0941
+3944**



**J1406
-0154**



Searching for X-Shaped Galaxies Hosting Binary Supermassive Blackholes

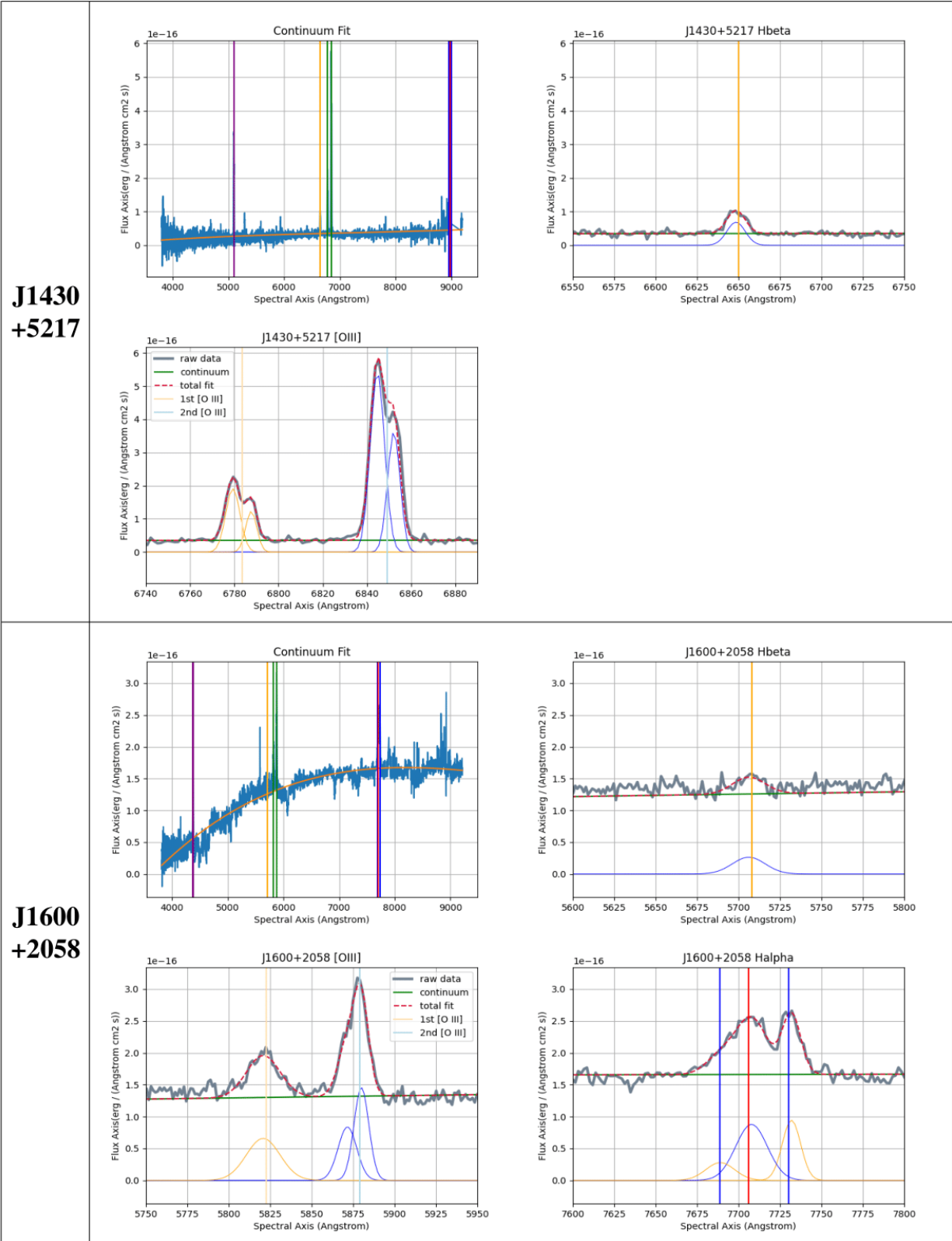


Figure 5 Binary XRG candidates' spectral plots with each XRG having their entire spectra on the top left, their H β emission on the top right, their [O III] emission on the bottom left, and their H α emission on the bottom left—for those with H α data available.

Table 2 Binary XRG Decompose Spectral Plot Parameters

XRG Name	Curve Description	Reduced Chi ²	Amplitude (E-16 erg/A/cm ² /s)	Amplitude Error (E-16 erg/A/cm ² /s)	Mean (Angstrom)	Mean Error (Angstrom)	Stdev (Angstrom)	Stdev Error (Angstrom)
J0036+0048	H _β	0.00103834	0.138	0.021	7737.25	1.15	5.72	0.93
	Right [OIII] (1)		1.774	0.076	7972.59	0.22	3.25	0.15
	Right [OIII] (2)	0.00407435	1.112	0.082	7961.26	0.67	4.67	0.22
	Left [OIII] (1)		0.562	0.069	7896.67	0.72	3.30	0.49
	Left [OIII] (2)		0.397	0.078	7884.93	1.68	4.43	0.60
J0220-0156	H _β	0.02007783	1.402	0.117	5705.64	0.45	4.11	0.36
	Right [OIII] (1)		3.026	1.931	5881.53	0.76	1.02	1.05
	Right [OIII] (2)	0.0786311	7.734	0.477	5875.36	0.47	3.57	0.14
	Left [OIII]		2.772	0.216	5819.99	0.45	4.49	0.37
	Right [NII]		1.405	0.093	7725.37	0.72	5.87	0.69
	Narrow H _α	0.0148851	3.409	0.272	7702.32	0.27	4.88	0.26
	Broad (left) H _α		0.912	0.104	7686.52	3.95	15.58	1.83
J0914+1715	Narrow H _β	0.000573624	0.181	0.034	7392.80	0.77	3.05	0.54
	Broad H _β		0.091	0.038	7383.00	3.50	4.16	0.90
	Right [OIII] (1)		1.816	0.094	7615.75	0.10	3.03	0.10
	Right [OIII] (2)	0.00119124	1.075	0.071	7606.33	0.69	5.17	0.14
	Left [OIII] (1)		0.440	0.144	7544.00	0.96	2.41	0.38
	Left [OIII] (2)		0.392	0.056	7535.37	1.99	6.89	0.54
	Right [NII]		0.224	0.076	10008.10	4.61	8.25	4.43
	H _α	0.0119221	0.475	0.056	9975.20	2.29	11.41	2.12
J0917+0523	Left [NII]		0.373	0.199	9951.17	3.50	1.39	0.60
	H _β	0.00107726	0.098	0.029	7740.27	1.72	3.98	1.15
	Right [OIII] (1)		0.161	0.066	7983.39	1.54	1.77	0.65
	Right [OIII] (2)	0.00139592	0.631	0.033	7973.25	0.59	5.49	0.26
J0941+3944	Left [OIII] (1)		0.081	0.151	7904.62	2.51	2.87	2.25
	Left [OIII] (2)		0.237	0.145	7895.87	5.31	3.96	0.55
	H _β (1)	0.000573624	1.814	0.860	5386.34	0.56	2.52	0.68
	H _β (2)		0.707	0.667	5381.29	6.02	1.44	0.42
	Right [OIII] (1)		20.655	2.369	5548.92	0.05	2.17	0.04
	Right [OIII] (2)	0.0775938	14.525	2.304	5543.64	0.87	2.00	0.04
	Left [OIII] (1)		6.515	1.255	5495.66	0.17	2.16	0.11
	Left [OIII] (2)		5.045	1.231	5490.69	1.27	2.00	0.12
	Right [NII]		4.928	0.143	7293.12	0.18	4.72	0.15
	H _α (1)	0.0119221	5.424	1.011	7273.24	0.21	2.88	0.13
J1406-0154	H _α (2)		3.842	1.032	7266.79	1.68	2.87	0.24
	Left [NII]		1.622	0.164	7254.01	1.00	4.83	0.42
	H _β	0.000544621	0.060	0.021	7969.90	2.06	4.17	1.40
	Right [OIII] (1)		0.097	0.021	8223.49	1.50	3.66	1.07
	Right [OIII] (2)	0.000396312	0.282	0.028	8210.12	0.69	3.19	0.21
J1430+5217	Left [OIII] (1)		0.049	0.021	8147.84	2.41	3.41	1.57
	Left [OIII] (2)		0.094	0.015	8130.98	1.39	5.39	0.86
	H _β	0.00366167	0.684	0.036	6648.47	0.37	5.56	0.32
	Right [OIII] (1)		3.633	0.147	6852.19	0.10	2.81	0.06
J1600+2058	Right [OIII] (2)	0.00457289	5.417	0.172	6844.75	0.22	3.25	0.04
	Left [OIII] (1)		1.227	0.125	6787.65	0.27	2.52	0.17
	Left [OIII] (2)		1.913	0.139	6779.35	0.51	3.23	0.10
	H _β	0.00796774	0.264	0.032	5706.18	1.41	9.91	1.37
J1600+2058	Right [OIII] (1)		1.456	0.468	5880.01	0.93	4.48	0.85
	Right [OIII] (2)	0.0105216	0.838	0.531	5871.58	4.67	5.63	0.62
	Left [OIII]		0.658	0.036	5820.75	0.66	10.20	0.64
	[NII] right		0.942	0.092	7731.93	0.68	5.58	0.62
	Narrow H _α	0.00668503	0.878	0.287	7707.84	20.20	9.57	14.96
Broad H _α		0.278	1.774	7688.97	58.31	8.70	3.13	

Table 3 XRGs with Indicators of Binary SMBHs

Galaxy	Velocity Difference (km/s)	Velocity Difference Error (km/s)
J0036+0048	694	59
J0220-0156	369	54
J0914+1715	543	70
J0917+0523	568	184
J0941+3944	308	47
J1406-0154	910	97
J1430+5217	473	19
J1600+2058	505	285

Table 4 Binary XRG H α and H β Redshift Differences and AGN Velocities

XRG Name	z	σ_z	Curve Description	corresponding	corresponding	corresponding	corresponding	corresponding	corresponding
				z_{AGN}	$\sigma_{z,AGN}$	$(z_{AGN} - z)$	$\sigma_{(z_{AGN} - z)}$	v_{AGN}	$\sigma_{(v_{AGN})}$
J0036+0048	0.590880	0.000050	H β	0.591580	0.000242	0.000700	0.000242	209970	74006
			H β	0.173671	0.000092				
J0220-0156			Narrow H α	0.173633	0.000041				
			Broad (left) H α	0.171226	0.000601				
J0914+1715	0.520040	0.000044	Narrow H β	0.520726	0.000158	0.000686	0.000164	205589	49289
			Broad H β	0.518710	0.000720	-0.001330	0.000721	398761	216248
			H α	0.519961	0.000348	-0.000079	0.000351	23755	105222
J0917+0523	0.592188	0.000042	H β	0.592202	0.000353	0.000014	0.000356	4080	106638
J0941+3944	0.107496	0.000012	H β (1)	0.107990	0.000116	0.000494	0.000116	147999	34846
			H β (2)	0.106951	0.001239	-0.000545	0.001239	163426	371509
			H α (1)	0.108252	0.000032	0.000756	0.000034	226765	10303
			H α (2)	0.107270	0.000255	-0.000226	0.000256	67875	76652
J1406-0154	0.639930	0.000123	H β	0.639437	0.000424	-0.000493	0.000441	147697	132240
J1430+5217	0.367580	0.000018	H β	0.367614	0.000077	0.000034	0.000079	10310	23681
J1600+2058	0.173860	0.000021	H β	0.173782	0.000291	-0.000078	0.000292	23408	87419
			Narrow H α	0.174474	0.003078	0.000614	0.003078	184112	922768
			Broad H α	0.171599	0.008885	-0.002261	0.008885	677880	2663641